Bulletin of the Seismological Society of America, Vol. 97, No. 1B, pp. 281–293, February 2007, doi: 10.1785/0120060120

Active Source Monitoring of Cross-Well Seismic Travel Time for Stress-Induced Changes

by Paul G. Silver, Thomas M. Daley, Fenglin Niu, and Ernest L. Majer

Abstract We have conducted a series of cross-well experiments to continuously measure *in situ* temporal variations in seismic velocity at two test sites: building 64 (B64) and Richmond Field Station (RFS) of the Lawrence Berkeley National Laboratory in California. A piezoelectric source was used to generate highly repeatable signals, and a string of 24 hydrophones was used to record the signals. The B64 experiment was conducted utilizing two boreholes 17 m deep and 3 m apart for ~160 h. At RFS, we collected a 36-day continuous record in a cross-borehole facility using two 70-m-deep holes separated by 30 m. With signal enhancement techniques we were able to achieve a precision of ~6.0 nsec and ~10 nsec in delay-time estimation from stacking of 1-hr records during the ~7- and ~35-day observation periods at the B64 and RFS sites, which correspond to 3 and 0.5 ppm of their travel times, respectively. Delay time measured at B64 has a variation of ~2 μsec in the 160-hr period and shows a strong and positive correlation with the barometric pressure change at the site. At RFS, after removal of a linear trend, we find a delay-time variation of ~2.5 μsec, which exhibits a significant negative correlation with barometric pressure. We attribute the observed correlations to stress sensitivity of seismic velocity known from laboratory studies. The positive and negative sign observed in the correlation is likely related to the expected near- and far-field effects of this stress dependence in a poroelastic medium. The stress sensitivity is estimated to be ~10^{-6}/Pa and ~10^{-7}/Pa at the B64 and RFS site, respectively.

Introduction

Measuring and monitoring changes in the subsurface stress field has been a long-sought goal of the geophysical community over recent decades. The monitoring of time-varying stress is a crucial diagnostic for at least two important fields of study: the nucleation and triggering of earthquakes and the distribution of reservoir fluids under the influence of withdrawal or injection. Knowledge of the subsurface stress field is currently inferred from surface measurements or single-point subsurface measurements. For example, geodesy provides important constraints on the surface deformation field, which can be related to seismogenic stress through an assumed structural model of the rheology, whereas borehole strainmeters can give point measurements of temporal variation in strain. Thus, the constraints on 3D spatial distribution of stress and strain from current measurements are limited. The surface constraints need to be combined with other techniques that, while not as directly related to stress and strain, have superior depth resolution. For example, temporal variations in microearthquake activity represent changes in the radiated component of creep that clearly reflects the ongoing deformation of the subsurface (Nadeau and McEvilly, 1999, 2004; Rogers and Dragert, 2003; Nadeau and Dolenc, 2005). Indeed, patterns of seismicity have long been used to make inferences about the stress state before and after seismic events (Bowman *et al.*, 1998). Similarly, changes in effective stress (background stress minus pore pressure) in reservoirs are typically inferred from point measurements in boreholes or surface measurements such as tilt. The measurement of *in situ* effective stress changes due to fluid withdrawal is a major focus of current exploration seismic studies (Sayers and Tura, 2005).

Numerous laboratory studies over several decades have shown that the elastic properties (e.g., seismic velocity, attenuation, and anisotropy) of crustal rocks clearly exhibit stress dependence (e.g., Birch, 1960, 1961; Scholz, 1968; Nur and Simmons, 1969). Theoretical studies have investigated the effects of cracks on seismic-wave propagation (e.g., O'Connell and Budiansky, 1974; Schoenberg, 1980; Hudson, 1981; Liu *et al.*, 2000). Stress dependence is usually attributed to the opening/closing of microcracks due to changes in the stress normal to the crack surface (e.g., Walsh, 1965; Nur, 1971; Crampin and Zatsepin, 1997).

Similarly, in porous reservoir rocks, the effective stress dependence of elastic properties has been attributed to compliant porosity (Shapiro, 2003). The coupling of elastic and fluid-flow-property dependence on effective stress changes has been modeled for fractured reservoirs (Daley *et al.*, 2006). Thus stress changes can, in principle, be detected by exploiting the stress sensitivity of elastic material properties. This stress dependence has been very difficult to detect *in situ*, however. There have been several attempts to accomplish this goal using active sources, especially in the 1970s after very promising laboratory studies, but with limited success (e.g., De Fazio *et al.*, 1973; Reasenberg and Aki, 1974; Leary *et al.*, 1979; Yukutake *et al.*, 1988).

An important component of *in situ* monitoring of stress with active-source seismic measurement is calibrating the change in seismic property (e.g., *P*- or *S*-wave velocity) with a known stress variation, such as earth tides or atmospheric pressure change. This would allow the identification of that part of seismic-velocity variation that is due to stress change in a given rock volume using an *in situ* determination of the stress-velocity relationship. Changes in seismic velocity induced by solid earth tidal loading and variations in barometric pressure have been estimated in some studies. The fractional change in seismic velocity with respect to stress change is reported to be in the range of 10^{-9}/Pa to 10^{-6}/Pa, depending on the environment of the experimental sites. Yet it is only very recently that compelling observations of delay-time change (i.e., velocity change over a fixed path) due to tides or barometric pressure have been made (Yamamura *et al.*, 2003; Sano, personal comm., 2004).

The major advances, compared with the earlier studies, are twofold. First, the characteristics of available seismic sources have significantly improved, primarily in repeatability. Detection of travel-time changes is maximized for highly repeatable sources that can operate at high frequency and for extended periods. Previous work used sources such as surface vibrators or air guns, which were difficult to keep running for extended periods and had limited repeatability. Modern piezoelectric borehole sources are highly repeatable and dependable for millions of source excitations. Second, the precision in measuring differential travel time has increased, made possible in large part by the greatly increased sample rates available with modern high-speed data-acquisition systems, and by the computational capability that permits massive waveform stacking. Additionally, the development of seismic sensors, both coil/magnet-type geophones and piezoelectric-type hydrophones has improved sensitivity and dependability over recent decades.

The recent observations of Yamamura *et al.* (2003) and Sano (personal comm., 2004) were made in an instrumented vault at a subsurface observatory and demonstrated that modern active-source seismic equipment has the precision and repeatability necessary to monitor stress for extended periods (months to years). A logical next step is to take such measurements to field sites and use equipment that is designed for temporary deployment in wells of opportunity. By using such wells, the *in situ* stress response can be monitored to assess the sensitivity. In this article we present results from *in situ* stress monitoring using typical shallow (10–100 m) field-site boreholes and equipment designed for cross-well seismic acquisition. First, we discuss stress sensitivity and measurability, and then we discuss our data-acquisition techniques. Finally, we present results from two field-scale experiments.

Stress Sensitivity and Measurability

Stress Sensitivity

The assumed physical basis for the stress sensitivity of seismic velocity in the crust is the presence of compliant material discontinuities, that is, cracks, fractures, joints, and faults (listed in increasing spatial size from microns to kilometers). These discontinuities are hereafter referred to as "cracks" because the most compelling observations to date are on the smaller scales, and because larger features are typically assumed to be treatable as assemblages of smaller fractures and cracks. There is good evidence that cracks are present to depths approaching 10 km (e.g., Huenges *et al.*, 1997). It is thus possible, in principle, to measure stress changes at these depths, assuming that velocity variations can be measured sufficiently precisely that this stress dependence can be calibrated in the same way that instruments can be calibrated, and that it is possible to account for sources of temporal variation unrelated to stress. Using an artificial source and fixed receivers, the simplest means of observing a time-dependent stress change is to measure the delay time between subsequent source pulses for the same path. The precision at which this measurement can be made determines the precision to which stress changes can be detected, and the interval between measurements determines the temporal resolution.

Assuming a distribution of cracks within a given volume, long wavelength theories lead to an equivalent elastic medium with fracture compliance tensor (e.g., Liu *et al.*, 2000). One crack property useful in determining compliance-dependent seismic velocity is the crack density ρ_c (e.g., Hudson and Liu, 1999). It is through the time dependence in ρ_c that we consider our attempt to observe the time dependence in stress. To quantify changes in seismic velocity, V, due to changes in stress, $\delta\sigma$, we define the stress sensitivity as $\eta = \delta\hat{v}/\delta\sigma$, where $\delta\hat{v}$ is the fractional velocity perturbation ($\delta V/V$) induced by the stress perturbation $\delta\sigma$. From a physical point of view, it is useful to express η as two terms involving crack density, $\eta = (\delta\hat{v}/\delta\rho_c)\,(\delta\rho_c/\delta\sigma)$, which reflect the seismological properties and stress sensitivity of a poroelastic medium, respectively.

Regarding seismic properties, in a classic article by O'Connell and Budiansky (1974), these authors developed a self-consistent approximation, where they consider the case of an isolated crack, and then account for crack interactions through the use of an effective Poisson's ratio that is the result of the presence of a population of cracks. There

have been other approaches to this problem (see Hudson, 2000, and references therein), which are in very good agreement at low crack densities, the range that will be most applicable to the measurement of seismogenic stress. $\delta\rho_c/\delta\sigma$ has been examined by several authors (e.g., Hudson, 2000; Tod, 2003). A deviatoric stress field will produce a crack density that is a function of orientation, leading to velocity anisotropy. The fracture's anisotropic elastic constants can be described in terms of a fracture-compliance matrix, which can be added to the compliance matrix of the host rock to find the equivalent-medium elastic constants (Schoenberg, 1980; Schoenberg and Sayers, 1995). Crack density and aspect ratio can be related to the fracture compliance matrix for aligned fracture sets (Hudson and Liu, 1999; Liu *et al.*, 2000), and the compliances of multiple fracture sets can be combined (Schoenberg and Sayers, 1995). Because the cracks within a given volume of rock are expected to have a range of aspect ratios and compliances, the sensitivity of crack density to stress consequently depends on the relative density of compliant cracks. In addition, because ρ_c is expected to be an exponentially decreasing function of confining pressure (e.g., Tod, 2003) and similarly, fracture compliance is expected to decrease exponentially with effective stress to an asymptote (Daley *et al.*, 2006), velocity sensitivity to stress is also expected to decrease exponentially with increasing depth. This places emphasis on high precision in measuring velocity perturbations.

Thus, if η is known and we observe $\delta\hat{v}$, then we can calculate stress variations. However, there can be complications. η is a function of crack fluid saturation through both $\delta\hat{v}/\delta\rho_c$ and $\delta\rho_c/\delta\sigma$ so that a change in fluid saturation could be interpreted as a change in stress. At this point we will assume we are working in fully saturated regions where only fluid pressure can change. As discussed by Hudson (2000) and Daley *et al.* (2006), one can treat the fluid pressure problem in terms of an apparent stress, defined as the externally applied stress minus the pore pressure.

While cracks constitute the physical basis for the stress sensitivity of seismic velocity, they are very difficult to observe directly. As a result, it has been customary to look to laboratory experiments or field experiments as a way of constraining η empirically. For example, in the experiment by Nur and Simmons (1969), they found that η is approximately 10^{-8}/Pa for both P and S waves under dry conditions over the pressure range of 0 to 30 MPa. For saturated cracks, we expect the same result for V_s and roughly half this value for V_p, which is what was approximately observed by laboratory experiments on fluid-saturated cracks (Nur and Simmons, 1969). η has also been estimated from field experiments. As summarized by Yamamura *et al.* (2003), in studies where authors have reported seeing tides, there is a large range of estimated values for η, which range from 10^{-6}/Pa (De Fazio *et al.*, 1973) to 10^{-9}/Pa (Sano *et al.*, 1999), with several values in between (see table 1 of Yamamura *et al.*, 2003). This range of three orders of magnitude could easily be related to variations in crack aspect ratio, high crack density near the surface, or variation of fluid saturation. This variability points to the importance of obtaining a reliable stress calibration for a given *in situ* rock volume.

Stress Measurability Using Travel Time

Using a fixed source–receiver pair, we can measure the stress-induced fractional change in seismic velocity, $\delta\hat{v}$, through the fractional change of travel time $\delta\hat{T}$. The relationship between the two can be written as $\delta\hat{T} = \delta\hat{L} - \delta\hat{v}$, where $\delta\hat{L} = \delta L/L$ is the fractional change in baseline length, $\delta L/L$. For distributed elastic strains in the crust, we expect the stress sensitivity of $\delta\hat{L}$ to be of order 10^{-11}/Pa, while the stress sensitivity of $\delta\hat{v}$ is orders of magnitude higher, or about 10^{-8}/Pa. Thus, for tidal and barometric stresses $\sim 10^3$ Pa we expect $\delta\hat{v}$ to be of order 10^{-5}, while $\delta\hat{L}$ should be proportional to strains, which will be of the order 10^{-8} and small compared with $\delta\hat{v}$. For such cases, $\delta\hat{v}$ can be estimated by measuring the lag time, τ, between two seismograms, i.e., $\delta\hat{v} = \tau/T$. In the case of nonelastic strain, such as slow slip on a fault, it is then possible for $\delta\hat{L}$ to dominate.

If we express both τ and T in terms of the characteristic frequency, f_0, $\tau = \varepsilon/f_0$, $T = N/f_0$, where N is the number of wavelengths between the source and receiver and ε is the normalized delay time, then the velocity perturbation, $\delta\hat{v}$, can be simply rewritten as the ratio of two dimensionless parameters:

$$\delta\hat{v} = \varepsilon/N. \tag{1}$$

This particular parameterization provides a simple way of scaling experiments both in terms of frequency and spatial extent.

From equation (1), it is clear that achieving the lowest possible detection threshold for $\delta\hat{v}$ can be broken into two separate tasks: (1) maximizing the number N of wavelengths between source and receiver, and (2) increasing the precision in measuring normalized delay time, ε (effectively the phase). The first task, maximizing N, is a property of the medium, the geometry, and the source characteristics, because N can be written as $N = Lf_0/V$. Thus, the acquisition geometry (path length) and characteristic frequency (which is a function of source output and the medium's attenuation), will factor into determining N. The medium is site dependent and not controllable; therefore, maximizing N is in the realm of data acquisition discussed subsequently. For our experiments, values of N will range from 10 to about 50.

The second task, minimizing ε, raises important questions about what controls the precision and to what extent can we obtain subsample precision through interpolation. The study of time delay estimation (TDE) is the critical data-analysis tool to answer these questions and has important applications in many fields, such as ultrasonic imaging in medical sciences. Therefore the performance of various TDE techniques and their achievable precisions are topics that

have been well studied. Theoretically, a lower bound exists that places a limit on the performance of all unbiased time-delay estimators. This limit is known as the Cramer-Rao Lower Bound (CRLB) (e.g., Carter, 1987; Walker and Trahey, 1995). It predicts the standard deviation of delay-time errors, σ_τ:

$$\sigma_\tau \geq \sqrt{\frac{3}{2 f_0^3 \pi^2 T(B^3 + 12B)} \left\{ \frac{1}{\rho^2}\left(1 + \frac{1}{\mathrm{SNR}^2}\right)^2 - 1 \right\}}, \tag{2}$$

when two seismograms are relatively similar. Here, f_0, B, ρ, SNR, and T are the center frequency, fractional bandwidth, source waveform correlation coefficient, signal-to-noise ratio, and kernel window length, respectively. In our case, $B < 1$, $\rho \approx 1$, SNR $\gg 1$, so that equation (2) can be further simplified. Expressing the uncertainty in terms of ε,

$$\sigma_\varepsilon = \sigma_\tau f_0 \geq \frac{1}{2\pi \cdot \mathrm{SNR}} \sqrt{\frac{1}{f_0 TB}} \sim \frac{1}{2\pi \cdot \mathrm{SNR}}, \tag{3}$$

since $(f_0\, TB)^{1/2}$ is of the order unity in our application. Equation (3) makes two very important points. First, the SNR is the only parameter that controls the relative precision in TDE. For example, the SNRs for a single record and for 100 stacked records from the first test site are ~300 and ~3000, respectively. The resulting predicted precision is on the order of 10^{-3} and 10^{-4}. These values correspond to errors of 10^{-7} sec and 10^{-8} sec in the delay-time estimates, which will be shown to be in good agreement with our measurements. Second, the precision is not affected by sampling rate, as long as the digitizing error is much smaller than other sources of noise. This provides the theoretical basis for achieving subsample precision through interpolation.

Several methods allow us to measure the delay time to subsample precision. We have tested three different cross-correlation-based algorithms: (1) cosine fitting, (2) seismogram interpolation, and (3) cross-correlation interpolation. Cosine curve fitting (method 1) has been used extensively in the past in interpolating the discrete correlation function to estimate subsample delay time (de Jong *et al.*, 1990, 1991; Cespedes *et al.*, 1995). In algorithm (2) we calculate the Fourier transform of a time series, pad the frequency spectrum with zeros, and calculate the inverse Fourier transform. In the preceding example, the data are interpolated to an interval of 10^{-8} sec. We then calculate the cross correlation between two seismograms. In method (3) the cross correlation is first calculated and then interpolated to a finer sampling interval (10^{-8} sec). In calculating the delay time between seismograms with high SNRs, all three algorithms yielded the same standard deviation of the mean delay time, of the order 10^{-9} ~10^{-8} sec.

As shown in equation (3), we can obtain better time-delay estimation by improving the SNR. A classical way to enhance SNR is stacking, which can improve the SNR by a factor of $N^{1/2}$ when the noise among traces is uncorrelated. We have extensively stacked the data and investigated whether the $N^{1/2}$ rule works for our case. Figure 1a shows an example of a single and a stacked waveform. Because of the high SNRs, the top two traces appear to be identical. However, a blowup of the first part of the single and stacked seismograms shows the expected factor of 10 improvement in SNR, in this case, from about 300 to 3000, which translates to an order of magnitude improvement in delay-time precision. The $N^{1/2}$ improvement works to stacking of at least 10,000 traces (Fig. 1b). The massive stacking allows us to obtain an SNR of 10^4–10^5 from one-hour recordings, corresponding to σ_ε on the order of 10^{-5} and 10^{-6} and detectability of $\delta\hat{v}$ on the order of 10^{-6} and 10^{-7}.

The CRLB expression (3) can be used to determine a characteristic frequency or, alternatively, a measurement distance that maximizes the precision in $\delta\hat{v}$. The CRLB tells us that ε and N in equation (1) are not entirely independent parameters, because ε depends on N through the influence of attenuation on SNR. By the definition of attenuation, signal amplitude is proportional to $(1 - \pi/Q)^N$. Using (3), then, the standard deviation of ε/N is proportional to $(1 - \pi/Q)^{-N} N^{-1}$. One can then find an optimal value for N that minimizes ε/N by differentiating this expression with respect to N and setting it equal to zero. For $\pi/Q \ll 1$, we find $N \sim Q/\pi$. Thus, there is an optimal value of N that effectively defines an optimal frequency band for every distance. For example, if $Q = 60$ ($N = 20$), and assuming the P velocity is 1.5 km/sec, the optimal frequencies for source–receiver distances of 3 m, 30 m, 100 m, and 1000 m (corresponding to the distance range that we expect to encounter) are 10 KHz, 1.0 KHz, 330 Hz, and 33 Hz, respectively. To the extent possible, we use the optimal frequency in the data-acquisition design. For our two test sites we were able to use 10 kHz and 1 kHz at 3 and 30 m, respectively. The analysis at our two test sites shows that we can achieve $\sigma_\varepsilon \sim 10^{-5}$ for a one-hour measurement interval. Thus we expect the detectable $\delta\hat{v}$ to be of the order 10^{-6}.

We believe that stresses induced by the solid Earth tides and barometric pressure are ideal to calibrate the stress sensitivity of velocity variations. Both the solid Earth tides and barometric pressure produce stress variations in the range of 10^2–10^3 Pa, which will cause a velocity perturbation, $\delta\hat{v}$, in the range of 10^{-3} to 10^{-5}, based on the η values observed from laboratory and field experimental measurements, and thus are in principal, measurable with our *in situ* cross-well experiments. We will focus on the utilization of barometric pressure for calibration, because there are sources of noise at 24-hr period, such as temperature fluctuations, that can easily mask tidal variations. By contrast, barometric pressure is a broadband signal with a peak in energy at about 6 days, which is well away from the daily cycle.

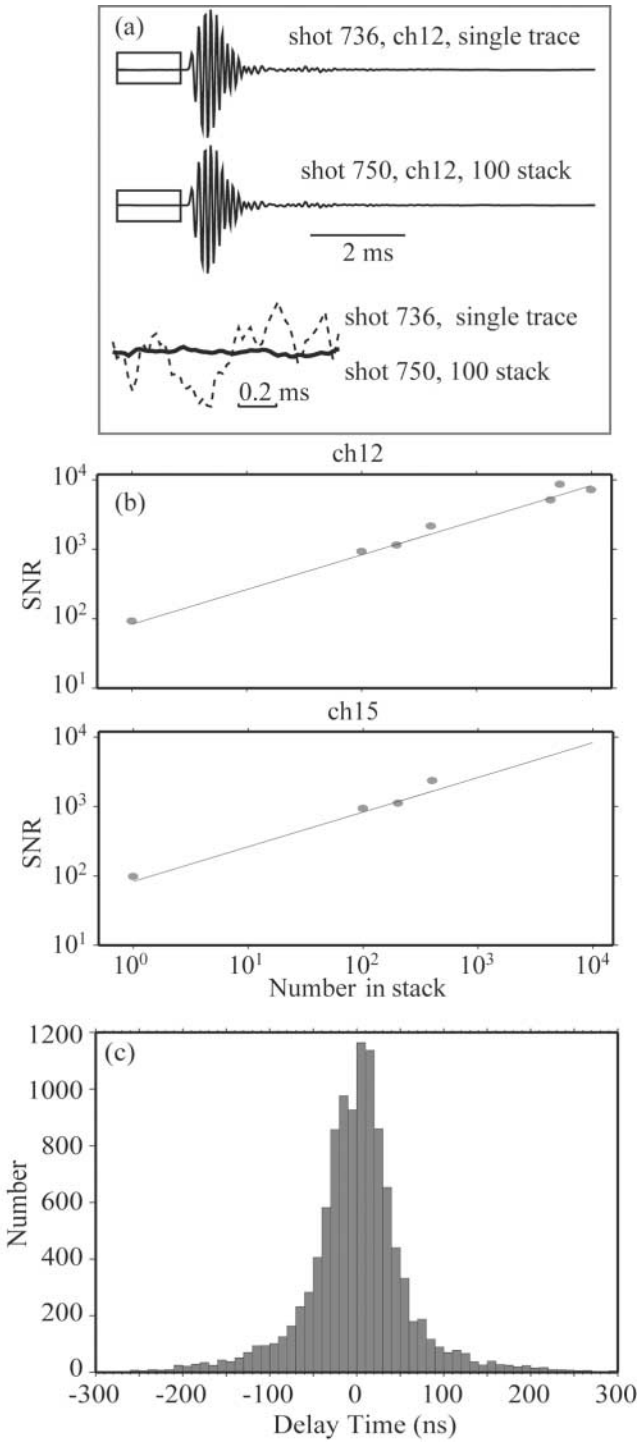

Figure 1. (a) Waveforms of a single shot (top trace) and a stack of 100 shots (middle trace) recorded by channel 12 at the B64 site. A comparison of the noise level of the two records is shown in the bottom. The noise windows, indicated by the boxes, of the two traces (with the solid and dashed lines indicating the stacked and single traces, respectively) are superimposed with true relative amplitude to the *P* arrivals. Note the dramatic reduction in noise level in the stacked record. (b) SNRs are plotted as a function of the number of traces stacked for two data channels, 12 (top) and 15 (bottom). The straight lines indicate an improvement of $N^{1/2}$ for noncoherent background noise. Agreement with the $N^{1/2}$ rule indicates that the noise is random and uncorrelated, rather than systematic. (c) Histogram of the measured delay time between two adjacent one-minute records for data from the B64 site.

Data Acquisition

Data Acquisition Overview

Data acquisition for continuous cross-well monitoring builds on development of cross-well seismic work of the previous 10–20 years, which was usually designed for tomographic imaging (e.g., Rector, 1995; Majer *et al.*, 1997; Daley *et al.* 2004) but more recently has been used for time-lapse monitoring (e.g., Hoversten *et al.*, 2003; Vasco, 2004). Three major data-acquisition components are involved: seismic source, seismic sensor, and the recording system. Our acquisition was conducted with a combination of commercial and specially built equipment. The specially built components are the piezoelectric source and the high-voltage amplifier used to power it. The source consists of cylindrical rings of piezoelectric ceramic (lead zirconate titanate) epoxied together and wired for positive and negative voltage on the inner and outer surfaces. This type of source has been used in many seismic cross-well surveys (e.g., Majer *et al.*, 1997; Daley *et al.*, 2004) and is known to be repeatable and dependable. The tests reported here used a single-cycle square wave generated by a source–waveform generator (in this case, a programmable analog signal generator), which also sends a trigger signal to the recording system. The sensors were commerical hydrophones designed for large bandwidth and high sensitivity using piezoelectric film and built-in amplifiers with analog data transmission to the surface recording system.

The commerical recording system, a "Geode" manufactured by Geometrics, has a 24-bit analog-to-digital converter using a sigma-delta conversion algorithm. Our data were collected at a sampling rate of 48,000 samples per second. The triggering of the recording system for each shot is an important consideration. The digitizer is continually sampling the data, and receives a trigger that will in general be between two digitized samples. Including a section of pre-trigger data, the time series is interpolated and resampled, so that the time series begins at the time of the trigger. This start time is not exact, and, at a sampling rate of 48,000/sec, this time is computed to the nearest 20th of a sample (Geometrics Engineering, personal comm., 2005). Thus there is a delay-time measurement error that will be at most a 40th of a sample (half-way between samples), and the average error will be an 80th of a sample, assuming that the errors are uniformly distributed. This corresponds to an average error of 260 nsec per trigger. The error in the stacked data are smaller by a factor of $N^{1/2}$, assuming the errors are uncorrelated. For

$N = 36{,}000$ traces, as in our experiments, the error is thus 1.4 nsec for one-hour sampling, which is less than other sources of error.

3-m Scale: B64 Site

Our first test was conducted at an interwell distance of about 3 m between two 17-m-deep holes near building 64 (B64) in the Lawrence Berkeley National Laboratory (LBNL). The piezoelectric source was set in one borehole 11 m below the surface. The source power supply for this test was a commercial high-voltage pulser, made by Cober Electronics. The sensor cable had 24 sensors at 0.5-m spacing and was placed in the other hole, with the top sensor 4 m below the surface. All 24 sensors were recorded. The source was pulsed every 100 msec with a record length of 10 msec, which yields 10 traces per sensor per second. These individual traces were stacked in the acquisition system with a stacked set of 24 traces output every minute. A one-minute record is thus a stacked recording consisting of real-time stack of 600 single traces for each sensor. An example of a single shot record (no stacking) for all 24 sensors is shown in Figure 2. The signal-to-noise ratio is very high even without any stacking, especially for those sensors in the middle of the receiver string. The sensors near the surface (channels 18–24) had much lower signal level because they were above the water table in a much more attenuative medium. One advantage of using multiple receivers is that we can select channels to be analyzed to obtain σ_ε as low as possible.

In this 3-m experiment we continuously recorded a total of 160 hr starting from 12 November 2003. The SNRs average $\sim$4000 for the stacked one-minute records. The best achievable precision of ε, based on equation (3) is $10^{-5}\sim10^{-4}$. Figure 1b shows that SNR for this experiment continues to increase for up to 10^4 stacks, implying that a nonrandom noise "floor" has not been reached. Since the center frequency of the data f_0 is 10 KHz, the corresponding best achievable precision in delay time is $10^{-9}\sim10^{-8}$ sec, that is, a few nanoseconds. Figure 1c shows the histogram of the measured delay time between two ajacent one-minute records, which follows a normal distribution with a standard deviation of $\sim$50 nsec, about an order of magnitude larger than the CRLB. For one-hour stacked records, assuming the noise is random and uncorrelated, we can achieve a standard deviation, or precision, of 6 nsec, which corresponds to a resolution of 3×10^{-6} on the velocity perturbation, $\delta\hat{v}$, in good agreement with the previously stated expectation of 10^{-6}. Since the *P*-wave velocity at the test site is $\sim$1.5 km/sec, the travel time, *T*, is $\sim$2 msec. Our actual precision is probably better than this, because there is a contribution from actual stress-induced velocity perturbations in the histogram. The precision estimated here, however, does not include any nonrandom noise. Two important potential nonrandom noise sources are clock drift and error in trigger timing. Such systematic errors could lead to a long-term trend in TDE. If we assume that the digitizer's clock has an aging rate of several parts per million per year (a typical value for commercial electronics), the resulting error in TDE will be a few tenths of a nanosecond during the one-week observation. The precision value thus will not change significantly from our estimation, even with the nonrandom noise being considered. This nanosecond precision is the key to successful stress monitoring.

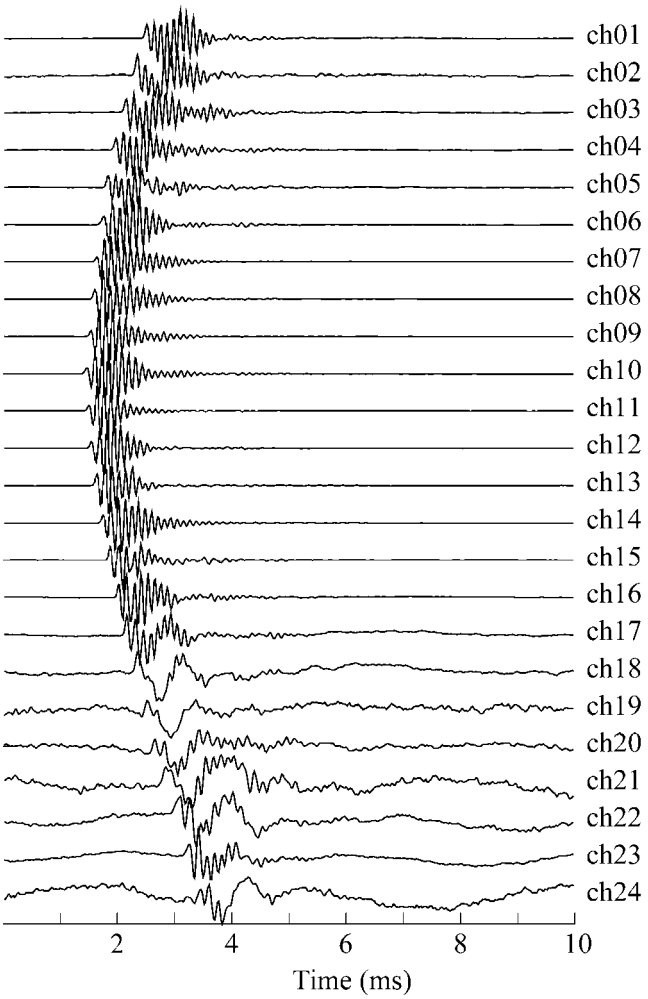

Figure 2. An example of cross-well seismograms for a single shot at the B64 test site. Channel 1 is at the bottom of the string, channel 24 is at the top.

30-m Scale: RFS Site

After the B64 site work, we wanted to deploy in deeper wells and at a greater interwell distance, hopefully moving out of the near-field well conditions at the B64. We chose to deploy in wells at the Richmond (California) Field Station (RFS), a test site on San Francisco Bay near the University of California, Berkeley. The RFS test site has several boreholes approximately 70 m deep and 30 m apart from each other (Daley and Gritto, 2001).

After initial testing in 2004 to choose and stabilize the acquisition equipment, the final monitoring was performed

in early 2005 (31 January to 23 March). A 4-inch piezoelectric source was set in one well (EMNE) 25 m below the surface, and the 24-element hydrophone array was placed in a nearby well (EMNW) at the depth range 25–36.5 m below the surface. The source high-voltage amplifier was custom made using IGBT (Integrated Gate Bipolar Transistor) technology. The high-voltage amplifier is designed to provide power for short-duration pulses to capacitive loads such as the piezoelectric ceramic. The source amplifier is broadband (500 Hz to over 10,000 Hz) and the input is a selectable waveform. At RFS the waveform was chosen to be a 1-msec-wide pulse (half-cycle of a square wave). The output waveform had 1.2 kV peak-to-peak amplitude. The source was repeated 10 times per second, with a 50-msec record length, and these pulses were stacked by the recording system to give recordings every 1 min (600 pulses). For this study, we attempted to reduce any movement of the sensors with "centralizers" (flexible bands of metal acting like springs) which kept three of the sensors fixed, and with hard foam attached to the source. The dominant frequency observed in the data was about 1 kHz and the travel time was about 20 msec (a V_p of 1.5 km/sec). Compared with the LBNL test, the data frequency is about 1/10, but the travel time is 10 times larger; therefore, we expected to achieve a resolution for $\delta\hat{v}$ that is essentially the same as the value we obtained at LBNL, $\sim 3 \times 10^{-6}$. The SNR of 1-min stacks is 604 with a standard deviation of 39.2 nsec, while 1-h stacks have a SNR of 3185 with 5.2-nsec standard deviation. We recorded 36 days of continuous data in the RFS test. If a clock drift of 5 ppm/year is taken into account, the precision for 36 days is about 10 nsec.

Data Analysis

3-m Experiment

In the 3-m experiment, we measured the delay time using two different time windows: a short-time window that includes the first arrival only (1.4 cycles) and a long-time window that includes the first arrival and coda (10 cycles). The measured delay times with respect to the trace using the two time windows are plotted in Figures 3a and b. Both show a time variation of ~ 3 μsec (for a travel time, ~ 2 msec), corresponding to $\delta\hat{v}$ of 10^{-3}. We also show the variations in barometric pressure (Fig. 3c) and dilatation (Fig. 3d) recorded by a nearby strainmeter. During the period of observation, we see a large pressure excursion ($\sim 10^3$ Pa) that continues for 3 days (Fig. 3c). It is very clear that the delay times closely track this barometric pressure change. Using the variations in delay time (from the coda) and the barometric pressure change, we obtain a value of stress sensitivity of $\eta = 10^{-6}$/Pa. Cross correlations between delay time with barometric pressure look very similar to the autocorrelation of the delay time with itself, demonstrating that at least at long period, there is an excellent correlation (Fig. 3e, 3f, and 3g). We also observed some small periodic peaks (3a) from delay times based on first arrivals only that have a 24-hr period. The Fourier spectra of the delay times (both first-arrival and complete waveform time series) and the dilatational strain data show the long-period barometric response. We can observe the diurnal and semidiurnal tidal signals in the strain data. The same components are also suggested in the delay time (first arrival). However, because of possible thermal noise at the 24-hr period (see below), we do not discuss these 24-hr signals further.

The sign of the travel-time fluctuation relative to the barometric pressure (increasing travel time for increasing pressure) is the opposite of standard expectation and requires some explanation. Under dry conditions, we expect increased barometric pressure to correspond to decreased travel time. The increased barometric load serves to close cracks, thus reducing crack density and increasing seismic velocity. The LBNL experiment is under wet conditions, however. The source and receivers are in 17-m-deep, water-filled boreholes that are likely in communication with the local aquifer. Under these conditions, it is possible to get either a positive or negative response to barometric pressure, depending on the barometric efficiency and the spacing between the source and receiver. For any significant barometric efficiency, a barometric pressure increase will increase the pressure in the well with respect to the aquifer, and this will induce flow to the aquifer until the wellhead pressure is in equilibrium with the pore pressure in the aquifer (Roeloffs, 1996). This leads to the often-observed drop in well water level with increasing barometric pressure, which additionally increases the pore pressure in the aquifer near the borehole, decreases the effective stress, and can lower seismic velocity. Therefore a measurement in the near field of a fluid-filled borehole in porous, permeable material (such as our 3-m LBNL test) could measure effective stresses of opposite sign to far-field barometric stress. Qualitatively, this provides a reasonable explanation for our initial observations. More detailed analyses, such as quantitative modeling of these data within the context of a poroelastic medium would require the measurement of other parameters, in particular, water-level data, to fully understand the relationship between delay-time data and stress in the near-well environment. As measured, the velocity-stress sensitivity at B64 is found to be 10^{-6}/Pa, which is in good agreement with previous and recent field experimental results (De Fazio *et al.*, 1973; Reasenberg and Aki, 1974; Leary *et al.*, 1979; Yamamura *et al.*, 2003; see table 1 in Yamamura *et al.*, 2003).

30-m Experiment

Continuous data were recorded at RFS for about 36 days. The estimated time delay is shown in Figure 4. During the 30-m experiment we found that ambient surface temperature had a measurable effect on the data. We observed that delay time correlates with temperature. The recording of temperature inside the recording container allowed correction for temperature variation. The scaling is

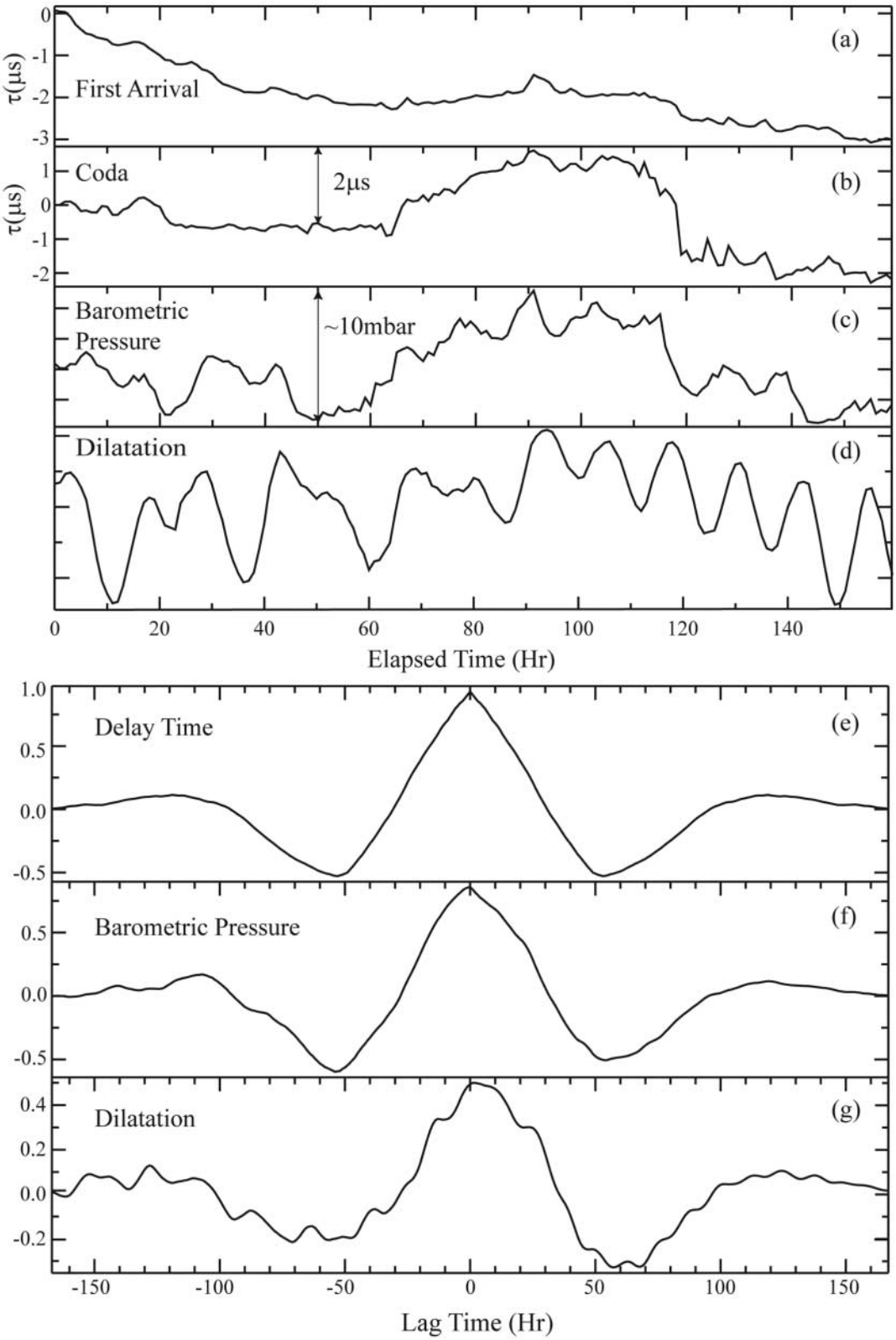

Figure 3. Delay times for the B64 test site estimated from time windows that contain the first arrival only (a), and the first arrival plus the coda (b) are shown with the barometric pressure (c) and dilatational strain data from a nearby strainmeter (d). Autocorrelation of the delay time and its cross correlations with barometric pressure and dilatation data are shown in (e), (f), and (g), respectively.

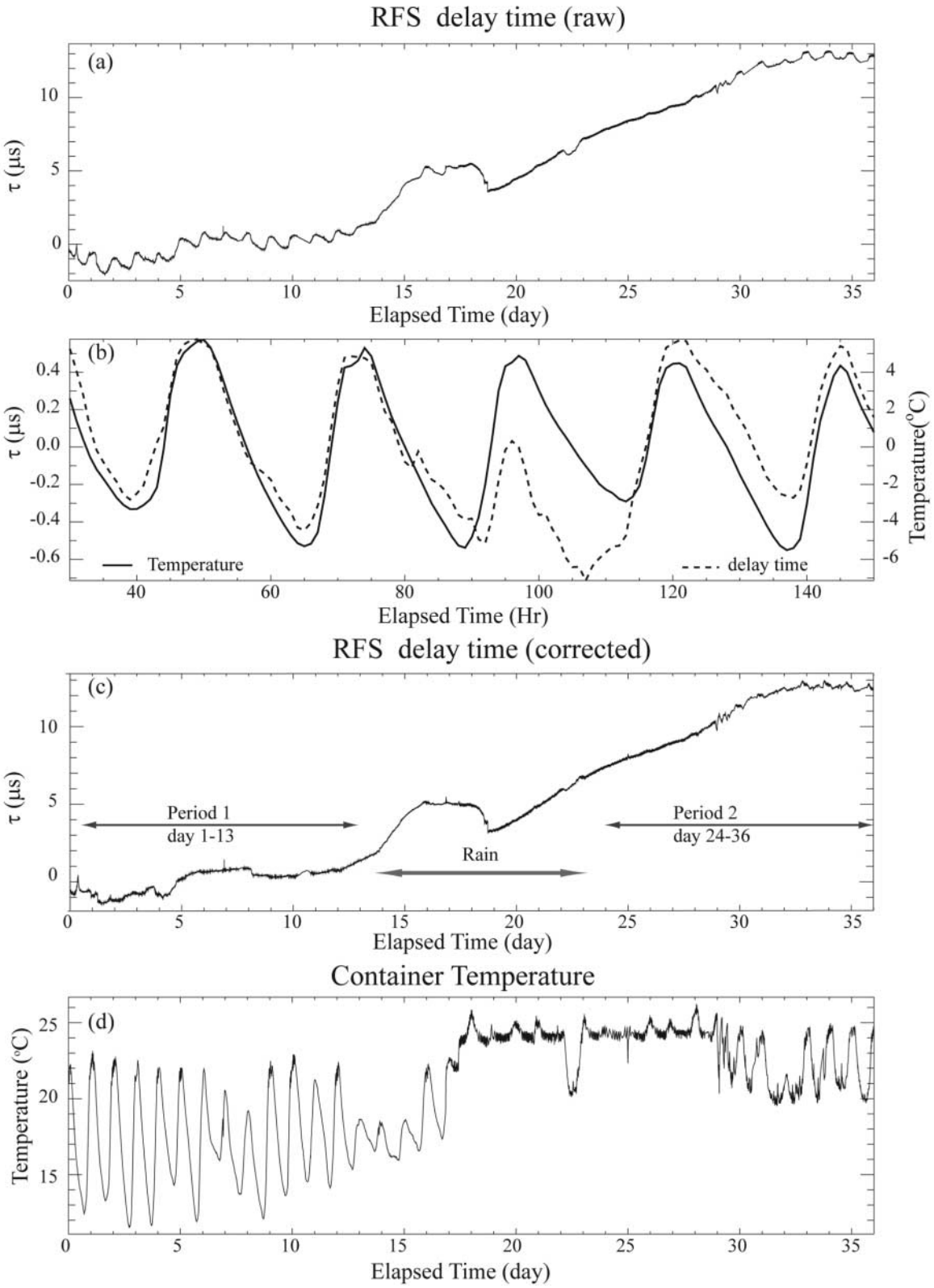

Figure 4. (a) Estimated delay time at RFS site over the 36-day period. (b) A comparison of delay-time and temperature data for the first 150 hr. (c) Delay-time data after a temperature correction of 0.1 μsec/°C. The record was divided into three periods: the rain period and the periods before and after it. (d) Temperature was measured in the container during the entire period.

about 0.1 μsec/°C as shown in Figure 4b, where swings of 10°C correspond to oscillations in delay time of about a microsecond. This is a large error, which we have treated in two ways. First, we can solve for a temperature-correction coefficient and subtract out this effect, assuming it is linear. A linear scaling constant between the measured temperature and the delay-time variation was estimated and the scaled temperature data were then subtracted from the delay-time data. This was effective in minimizing the daily cycle in delay time due to temperature, as seen in Figure 4c. Second, we can minimize the effect by maintaining the electronics within a temperature range, which was done midway through the experiment, also seen in Figure 4d.

As seen in Figure 4c, there is a large linear trend in the data, and a large excursion from day 13 to 19. We do not know the cause of this trend, but have removed it for further analysis, because we are interested in higher-frequency signals, in particular, the 6-day period of barometric pressure. The large excursion in the middle of the interval is most likely due to rainfall, because it coincides with an extended period of rain starting on day 14 and lasting until day 21. Because this signal is in the frequency band of interest, we interpret our data only before and after this period corresponding to days 1–13 and 24–36 (Fig. 5). The delay time with both the temperature effect and linear trend removed for the two periods (Fig. 5a and c) are shown with barometric pressure (Fig. 5b and d). We observed a delay-time change of $\sim$1 μsec corresponding to a barometric pressure change of $\sim$15 millibars in the first period, leading to an estimate of $\delta\hat{v} \sim 5 \times 10^{-5}$, and a stress sensitivity η of $\sim 5 \times 10^{-8}$/Pa. For the second period, changes in the delay time and barometric pressure are approximately 2.5 μsec and $\sim$10 millibars, respectively, which results in a η of $\sim 12.5 \times 10^{-8}$/Pa. The second period appears to have larger stress sensitivity, which might be due to weakening of medium resulting from the rain. Overall, the correlation between delay time and barometric pressure is significant at the 95% confidence level. Importantly, the sign of travel-time fluctuation relative to the barometric pressure is opposite to what we observed at LBNL, a decrease in travel time for increasing pressure (Figs. 5e and f). This is consistent with the expected far-field effect from barometric pressure.

The data from the period of significant rainfall are difficult to interpret. At least two possible effects could be involved: (1) an increase in surface load (increasing effective stress) due to the mass of the rainwater, and (2) an increase in pore pressure (decreasing effective stress) due to the infiltration of rainwater. These two effects make opposite predictions, with the surface-load effect tending to decrease delay time, and increasing pore pressure tending to increase delay time. Thus the sense of the excursion would be consistent with the latter effect.

Discussions and Conclusions

We found a good correlation between the delay time and barometric pressure in both the LBNL and RFS borehole sites. The sign of the correlation is, however, opposite in the two cases. Our preferred explanation for this difference is due to the dominance of a near-field effect at LBNL and a far-field effect at RFS. An increase in barometric pressure acting directly on the borehole will raise pore pressure, open cracks, and therefore increase crack density in the near-field region next to the borehole (Fig. 6). In the far field, the same increase in barometric pressure will close cracks and reduce crack density. The change in seismic velocity along a particular ray path thus depends on the net change in crack density. When two boreholes are relatively close, an increase of crack density and therefore a decrease of seismic velocity would be expected (Fig. 6).

The state-of-the-art in controlled source seismic acquisition has advanced to the point of measuring nanosecond variations in travel time. This precision allows *in situ* measurement of subsurface stress via the stress sensitivity of seismic velocity. The cross-well acquisition geometry provides access to the subsurface without the large variability associated with near-surface measurement. The use of removable equipment allows flexibility and cost savings in deployment. Importantly, natural stress signals such as barometric pressure or solid-earth tides provide a means to calibrate the stress sensitivity of a given rock volume.

We have presented a methodology for estimating the precision and describing the lower bound of SNR for a given experiment's parameters (source–receiver distance, signal frequency), thereby allowing selection of optimal acquisition parameters. In two separate field experiments, at two distance scales, we have shown the effect of barometric pressure on cross-well travel time and thereby calibrated the stress sensitivity of the rock volume between the wells. At the 3-m scale, the stress sensitivity appears to be controlled by near-well pore fluid pressure increase, which decreases effective stress in the rock for increasing barometric pressure. At the 30-m scale, travel-time measurement is dominated by a "far-field" region in which pore pressure is stable and increasing barometric pressure increases the effective stress. Quantitative analysis of the crossover between these two regimes requires a coupled hydromechanical model of the subsurface. In the 3-m experiment we found a stress sensitivity of 10^{-6}/Pa, whereas in the 30-m experiment the sensitivity was 5–12.5×10^{-8}/Pa. These calibration measurements provide the foundation for any long-term measurement of tectonic stress change, such as those associated with earthquake occurrence, or for varying stress change such as that due to fluid injection or withdrawal.

Acknowledgments

We thank Rob Trautz of LBNL for supplying the barometric pressure logger and helping with field work. We also thank Osamu Sano for helpful advices and discussions for designing our experiments. The Associate Editor, Robert Nowack, and two anonymous reviewers provided constructive reviews that improved the manuscript significantly. This work was supported by NSF Grants EAR-0352134 (to F.N.), EAR-0453471 (to F.N.), EAR-0352119 (to P.G.S.), and EAR-0453638 (to P.G.S.), and the Carnegie Institution of Washington, D.T.M. (to P.G.S.).

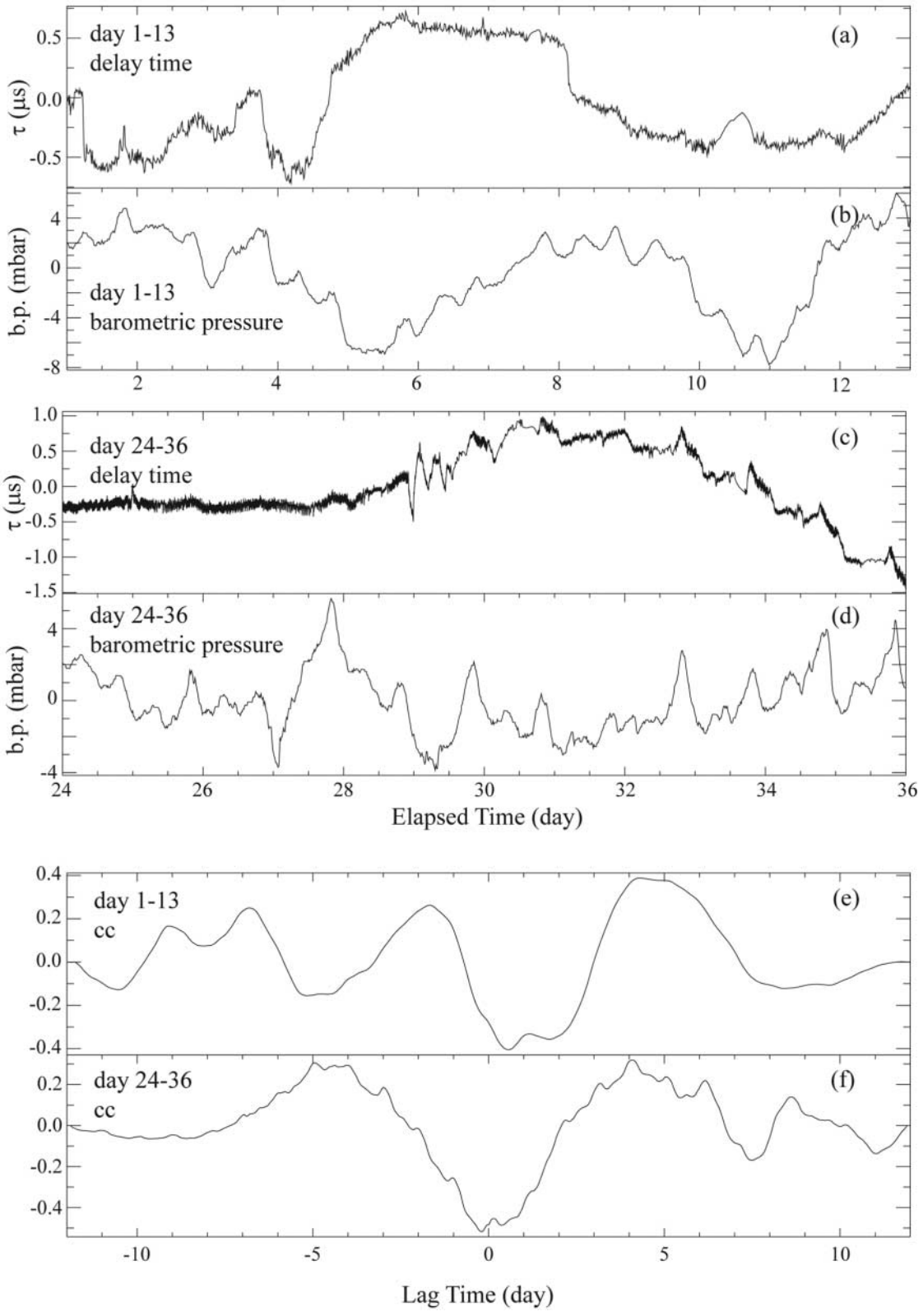

Figure 5. Delay time after temperature correction and a further removal of the linear trend in Figure 4 are shown with barometric data for days 1–13 (a and b) and 24–36 (c and d), respectively. There is a negative correlation between the delay time and pressure series for both periods (e and f). The correlation coefficients (cc) are -0.41 and -0.52 for the first and second period, and -0.40 for the combined period. Assuming one degree of freedom for each day of data, we find that the correlation is significant at the 95% confidence level.

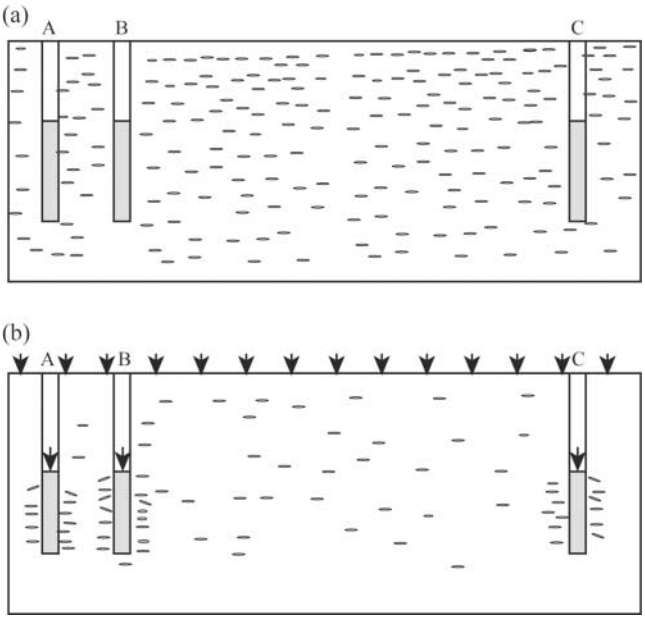

Figure 6. Schematic illustrating the near- and far-field effects of stress on open/closure of crack. (a) Initial distribution of cracks, which are shown by short solid lines. (b) Redistribution of cracks in response to an increase of barometric pressure. An increase (decrease) in crack density is expected for media near (far from) the borehole. The redistribution results in a net increase of crack density along path between boreholes A and B (near-field case) and a decrease along A and C (far-field case).

References

Birch, F. (1960). The velocity of compressional waves in rocks to 10 kilobars, part 1, *J. Geophys. Res.* **65,** 1083–1102.

Bowman, D. D., G. Ouillon, C. G. Sammis, A. Sornette, and D. Sornette (1998). An observational test of the critical earthquake concept, *J. Geophys. Res.* **103,** 24,359–24,372.

Carter, G. C. (1987). Coherence and time delay estimation, *Proc. IEEE* **75,** 236–255.

Cespedes, I., Y. Huang, J. Ophir, and S. Spratt (1995). Methods for estimation of sub-sample time delays of digitized echo signals, *Ultrason. Imag.* **17,** 142–171.

Crampin, S., and S. V. Zatsepin (1997). Modeling the compliance of crustal rock; II, Response to temporal changes before earthquakes, *Geophys. J. Int.* **129,** 495–506.

Daley, T. M., and R. Gritto (2001). Field test of INEEL tube-wave suppressor and LBNL borehole seismic system at Richmond Field Station, Lawrence Berkeley National Laboratory Report, February, LBNL-49015.

Daley, T. M., E. L. Majer, and J. E. Peterson (2004). Crosswell seismic imaging in a contaminated basalt aquifer, *Geophysics* **69,** 16–24.

Daley, T. M., M. A. Schoenberg, J. Rutqvist, and K. T. Nihei (2006). Fractured reservoirs: an analysis of coupled elastodynamic and permeability changes due to pore-pressure variation, *Geophysics* **71,** 33–41.

De Fazio, T. L., K. Aki, and J. Alba (1973). Solid earth tide and observed change in the in situ seismic velocity, *J. Geophys. Res.* **78,** 1319–1322.

De Jong, P.G.M., T. Arts, A.P.G. Hoeks, and R. S. Reneman (1990). Determination of tissue motion velocity by correlation interpolation of pulsed ultrasonic echo signals, *Ultrason. Imag.* **12,** 84–98.

De Jong, P.G.M., T. Arts, A.P.G. Hoeks, and R. S. Reneman (1991). Experimental evaluation of the correlation interpolation technique to measure regional tissue velocity, *Ultrason. Imag.* **13,** 145–161.

Hoversten, G. M., R. Gritto, J. Washbourne, and T. Daley (2003). Pressure and fluid saturation prediction in a multicomponent reservoir using combined seismic and electromagnetic imaging, *Geophysics* **68,** 1580–1591.

Hudson, J. A. (1981). Wave speeds and attenuation of elastic waves in material containing cracks, *Geophys. J. R. Astr. Soc.* **64,** 133–150.

Hudson, J. A. (2000). The effect of fluid pressure on wave speeds in a cracked solid, *Geophys. J. Int.* **143,** 302–310.

Hudson, J. A., and E. Liu (1999). Effective elastic properties of heavily faulted structures, *Geophysics* **64,** 479–485.

Huenges, E., J. Erzinger, J. Kueck, B. Engeser, and W. Kessels (1997). The permeable crust; geohydraulic properties down to 9101 m depth, *J. Geophys. Res.* **102,** 18,255–18,265.

Leary, P. C., P. E. Malin, R. A. Phinny, T. Brocher, and R. Voncolln (1979). Systematic monitoring of millisecond travel time variations near Palmdale, California, *J. Geophys. Res.* **84,** 659–666.

Liu, E., J. A. Hudson, and T. Pointer (2000). Equivalent medium representation of fractured rock, *J. Geophys. Res.* **105,** 2981–3000.

Majer, E. L., J. E. Peterson, T. M. Daley, B. Kaelin, L. Myer, J. Queen, P. D'Onfro, and W. Rizer (1997). Fracture detection using crosswell and single well surveys, *Geophysics* **62,** 495–504.

Nadeau, R. M., and D. Dolenc (2005). Nonvolcanic tremors deep beneath the San Andreas fault, *Science* **307,** 389.

Nadeau, R. M., and T. V. McEvilly (1999). Fault slip rates at depth from recurrence intervals of repeating microearthquakes, *Science* **285,** 718–721.

Nadeau, R. M., and T. V. McEvilly (2004). Periodic pulsing of characteristic microearthquakes on the San Andreas Fault, *Science* **303,** 220–222.

Nur, A. (1971). Effects of stress on velocity anisotropy in rocks with cracks, *J. Geophys. Res.* **76,** 2022–2034.

Nur, A., and G. Simmons (1969). The effect of saturation on velocity in low porosity rocks, *Earth Planet. Sci. Lett.* **7,** 183–193.

O'Connell, R. J., and B. Budiansky (1974). Seismic velocities in dry and saturated cracked solids, *J. Geophys. Res.* **79,** 5412–5426.

Reasenberg, P., and K. Aki (1974). A precise, continuous measurement of seismic velocity for monitoring in situ stress, *J. Geophys. Res.* **79,** 399–406.

Rector, J. W., III (1995). Croswell methods: where are we, where are we going?, *Geophysics* **60,** 629–630.

Roeloffs, E. A. (1996). Poroelastic techniques in the study of earthquake related hydrologic phenomena, *Adv. Geophys.* **37,** 135–195.

Rogers, G., and H. Dragert (2003). Episodic tremor and slip on the Cascadian subduction zone: the chatter of silent slip, *Science* **300,** 1942–1943.

Sano, O., K. Hieda, K. Hirano, T. Hirano, H. Ishii, Y. Hirata, S. Matsumoto, and T. Yamauchi (1999). Stress-sensitivity of the sound velocity at Kamaishi mine, Presented at Seismological Society of Japan 1999 Fall Meeting, Sendai, Japan.

Sayers, C., and A. Tura (2005). Introduction to this special section: rocks under stress, *The Leading Edge* **24,** 1213.

Schoenberg, M. (1980). Elastic wave behavior across linear slip interfaces, *J. Acoust. Soc. Am.* **68,** 1516–1521.

Schoenberg, M., and C. M. Sayers (1995). Seismic anisotropy of fractured rock, *Geophysics* **60,** 204–211.

Scholz, C. H. (1968). Microfracturing and the inelastic deformation of rock, I: Compression, *J. Geophys. Res.* **73,** 1417–1432.

Shapiro, S. A. (2003). Elastic piezosensitivity of porous and fractured rocks, *Geophysics* **68,** 482–486.

Tod, S. R. (2003). Bed-limited cracks in effective medium theory, *Geophys. J. Int.* **152,** 344–352.

Vasco, D. W. (2004). Seismic imaging of reservoir flow properties: time-lapse pressure changes, *Geophysics* **69,** 511–521.

Walker, W. F., and G. E. Trahey (1995). A fundamental limit on delay estimation using partially correlated speckle signals, *IEEE Trans. Ultrasono Ferroelect. Freq. Control* **42,** 301–308.

Walsh, J. B. (1965). The effect of cracks on the compressibility of rock, *J. Geophys. Res.* **70,** 381–389.

Yamamura, K., O. Sano, H. Utada, Y. Takei, S. Nakao, and Y. Fukao (2003). Long-term observation of in situ seismic velocity and attenuation, *J. Geophys. Res.* **108,** 2317, doi 10.1029/2002JB002005.

Yukutake, H., T. Nakajima, and K. Doi (1988). In situ measurements of elastic wave velocity in a mine, and the effects of water and stress on their variation, *Tectonophysics* **149,** 165–175.

Department of Terrestrial Magnetism
Carnegie Institution of Washington
5241 Broad Branch Road, N.W.
Washington, D.C. 20015
(P.G.S.)

Earth Science Division
Lawrence Berkeley National Laboratory
Berkeley, California 94720
(T.M.D., E.L.M.)

Department of Earth Science
Rice University
6100 Main Street
Houston, Texas 77005
niu@rice.edu
(F.N.)

Manuscript received 30 May 2006.